2023

Lightweight Co-free eutectic high-entropy alloy with high strength and ductility by casting

Wen Chen

et. al.

Recommended Citation

Chen, Wen and et. al., "Lightweight Co-free eutectic high-entropy alloy with high strength and ductility by casting" (2023). *Materials Research Letters*. 653.
https://doi.org/10.1080/21663831.2023.2284328

Materials Research Letters

ISSN: (Print) (Online) Journal homepage: https://www.tandfonline.com/loi/tmrl20

Lightweight Co-free eutectic high-entropy alloy with high strength and ductility by casting

Shuai Feng, Shuai Guan, Xiangkui Liu, Siyuan Peng, Kewei Dong, Yang Yang, Xinsheng Chen, Yuzheng Liang, Qipeng Wang, Yanfang Liu, Yong Peng, Kehong Wang, Wen Chen & Jian Kong

To cite this article: Shuai Feng, Shuai Guan, Xiangkui Liu, Siyuan Peng, Kewei Dong, Yang Yang, Xinsheng Chen, Yuzheng Liang, Qipeng Wang, Yanfang Liu, Yong Peng, Kehong Wang, Wen Chen & Jian Kong (2024) Lightweight Co-free eutectic high-entropy alloy with high strength and ductility by casting, Materials Research Letters, 12:1, 26-33, DOI: 10.1080/21663831.2023.2284328

To link to this article: https://doi.org/10.1080/21663831.2023.2284328

MATER. RES. LETT.
2024, VOL. 12, NO. 1, 26–33
https://doi.org/10.1080/21663831.2023.2284328

MATERIALS RESEARCH LETTERS
Taylor & Francis
Taylor & Francis Group

ORIGINAL REPORTS

Lightweight Co-free eutectic high-entropy alloy with high strength and ductility by casting

Shuai Feng[a], Shuai Guan[b], Xiangkui Liu[a], Siyuan Peng[c], Kewei Dong[a], Yang Yang[a], Xinsheng Chen[a], Yuzheng Liang[a], Qipeng Wang[a], Yanfang Liu[a], Yong Peng[a], Kehong Wang[a], Wen Chen[b] and Jian Kong[a]

[a]School of Materials Science and Engineering, Nanjing University of Science and Technology, Nanjing, People's Republic of China; [b]Department of Mechanical and Industrial Engineering, University of Massachusetts, Amherst, MA, USA; [c]Fujian Key Laboratory of Functional Materials and Applications, School of Materials Science and Engineering, Xiamen University of Technology, Xiamen, People's Republic of China

ABSTRACT

We report a cast light-weight dual-phase eutectic high-entropy alloy (EHEA) of $Ni_{49}Fe_{28}Al_{17}V_6$ that comprises of alternating FCC and ordered B2 lamellae. Such lamellar EHEA exhibits a superior tensile strength of ~ 1.3 GPa in combination with a large uniform elongation of ~ 26%, well surpassing those of other state-of-the-art cast EHEAs. The high strength-ductility synergy originates largely from the extensive dislocation activities in both FCC and B2 lamellae. In addition, the martensitic transformation of the B2 lamellae during deformation further promotes the work hardening capability to enhance the tensile strength and ductility.

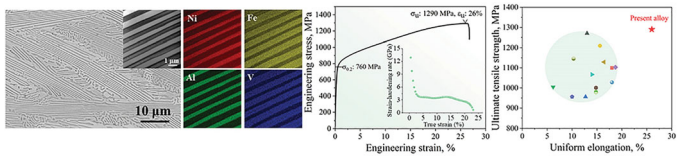

ARTICLE HISTORY
Received 6 September 2023

KEYWORDS
Eutectic high-entropy alloy; Lamellar structure; mechanical properties; strengthening mechanism; martensitic transformation

IMPACT STATEMENT

A novel cast $Ni_{49}Fe_{28}Al_{17}V_6$ eutectic high-entropy alloy comprised of FCC and B2 nanolamellae exhibits a remarkable combination of tensile strength and uniform elongation, well surpassing those of other state-of-the-art cast eutectic high-entropy alloys.

1. Introduction

Different from conventional alloys with a single base element, high-entropy alloys (HEAs) comprise multi-principal elements in equiatomic or near-equiatomic ratios and open a near-infinite compositional space for new material development [1–3]. The high configurational entropy of HEAs tends to overwrite the enthalpy of mixing and stabilize single-phase solid solution structures, especially at high temperatures or upon rapid cooling [4]. However, these single-phase HEAs often exhibit a limited strength-ductility combination [1,2]. To overcome this challenge, a class of eutectic high-entropy alloys (EHEAs) has been developed that typically possesses a dual-phase lamellar structure of alternating hard and soft phases, leading to a superior strength-ductility synergy [5,6]. For example, Lu et al. designed an EHEA of $AlCoCrFeNi_{2.1}$ which exhibits a lamellar structure of alternating disordered face-centered cubic (FCC) and ordered B2 phases [7]. The high strain-hardening capability of the FCC lamellae and the pinning effect of Cr-rich nano-precipitates in the B2 lamellae contribute to a superior ultimate tensile strength of ~ 1080 MPa together with a large ductility of ~ 16% [8]. In addition, similar to conventional eutectic alloys, EHEAs exhibit excellent castability and macroscopic homogeneity, making them feasible for mass production [5,7]. However, most existing EHEAs, including $AlCoCrFeNi_{2.1}$, contain a large amount of expensive and resource-critical Co elements [5], which seriously restricts their widespread applications. Furthermore, many EHEAs contain heavy

CONTACT Shuai Guan shuai.guan@connect.polyu.hk; Wen Chen wenchen@umass.edu Department of Mechanical and Industrial Engineering, University of Massachusetts, Amherst, MA 01003, USA; Jian Kong kongjian68@126.com School of Materials Science and Engineering, Nanjing University of Science and Technology, Nanjing 210094, People's Republic of China

Supplemental data for this article can be accessed online at https://doi.org/10.1080/21663831.2023.2284328.

refractory alloying elements (e.g. Ta and W), which lead to a relatively high density (> 7 g/cm^3) and triggers the formation of undesired low-symmetry constituent phases such as C14-type Laves phase [5,9–14]. These low-symmetry constituent phases have insufficient independent slip systems and are usually brittle [15].

In the present work, a novel $Ni_{49}Fe_{28}Al_{17}V_6$ EHEA with FCC/B2 lamellar eutectic microstructures was designed based on thermodynamic calculation of phase diagram (CALPHAD) using Thermo-Calc software with the TCHEA4 thermodynamic database paired with experimental methods [5]. Ni–Fe–Al–Co system was selected as the initial research target because it contains binary, ternary, and quaternary eutectic alloys among these constituent elements [16]. Then, we removed the expensive Co element and the Ni-Fe–Al system with the eutectic composition line is shown in Supplementary Figure S1. Within such target Ni-Fe–Al system, we introduced light V element, especially considering that light V element has a large atom radius and has been widely utilized for strengthening both FCC and BCC transition-metal based HEAs by providing strong solid-solution hardening via severe lattice distortion and large misfit volumes [17]. Then, CALPHAD tool was applied to narrow down the compositions close to the eutectic line. In addition, some trial-and-error experiments were subsequently carried out to achieve the exact eutectic composition of $Ni_{49}Fe_{28}Al_{17}V_6$. The directly cast $Ni_{49}Fe_{28}Al_{17}V_6$ exhibits a low density of $\sim$ 6.9 g/cm^3 with a nanolamellar eutectic structure comprised of alternating FCC and B2 phases, giving rise to a superior tensile strength of $\sim$ 1.3 GPa paired with a remarkable uniform elongation of $\sim$ 26%. Our post-mortem microstructural characterization reveals that the excellent strength-ductility synergy is attributed to the extensive dislocation activities in both FCC and B2 nanolamellae as well as the martensitic transformation-induced plasticity (TRIP) in the B2 nanolamellae.

2. Materials and methods

Alloy ingots with a nominal composition of $Ni_{49}Fe_{28}Al_{17}V_6$ (at.%) were prepared by arc-melting high-purity ($>$ 99.95 wt.%) metals in an argon atmosphere. The ingots were re-melted at least six times to ensure the chemical homogeneity and were subsequently drop cast into a $60 \times 10 \times 5$ mm^3 copper mold. Flat dog-bone-shaped tensile samples with nominal gauge dimensions of 8 mm (length) $\times$ 2 mm (width) $\times$ 1 mm (thickness) were cut based on ASTM E8 and mechanically polished to a metallurgical grit size of 1200. Tensile tests were performed on an Instron 5969 universal testing machine at a strain rate of 2×10^{-4} s^{-1} at room temperature. Tensile strain was monitored using a non-contact AVE2 video extensometer with a displacement resolution of 0.5 μm. At least three tensile samples were tested to ensure reproducibility. Phases were characterized by X-ray diffraction (XRD, Cu-K_α radiation, Bruker-AXS D8 Advance) measurement with a scan rate of 5 deg/min and a step size of 0.1 deg. The microstructure was examined by a field-emission high-resolution scanning electron microscope (SEM, Carl Zeiss-Auriga-45) integrated with an electron-backscattered diffraction detector (EBSD, Oxford Instruments Aztec 2.0 EBSD system). The EBSD data was acquired at a step size of 50 nm and was analyzed by Channel 5 software. Before SEM and EBSD analyses, the samples were mechanically polished using a 20 nm oxide polishing suspension, and the samples for SEM study were further etched in a solution of nitric acid, hydrochloric acid, and ethanol with a ratio of 1:3:8. Transmission electron microscopy (TEM) characterization was performed by an FEI Talos F200X instrument to reveal the microstructural features before and after tensile straining. Thin-foil specimens for TEM were prepared through mechanical polishing and ion milling to produce an electron-transparent zone. CALculation of PHAse Diagram (CALPHAD) approach was performed using Thermo-Calc software with the high-entropy alloys database (v. TCHEA4) to predict the phase equilibria.

3. Results and discussion

The equilibrium phase diagram of $Ni_{49}Fe_{28}Al_{17}V_6$ predicts that FCC/$L1_2$ and B2 phases are co-solidified from the melt within a very narrow temperature range of 1312 - 1314 °C (Figure 1a), indicative of a eutectic reaction. The mass fractions of FCC/$L1_2$ and B2 phases are predicted to be $\sim$ 75% and $\sim$ 25%, respectively. Such a phase constitution is further verified by our XRD pattern of the as-cast $Ni_{49}Fe_{28}Al_{17}V_6$ EHEA (Figure 1b), where only peaks corresponding to FCC/$L1_2$ and BCC/B2 phases are identified. The FCC and $L1_2$ phases were difficult to distinguish by XRD due to their similar lattice parameters. Similarly, it is also hard to distinguish BCC and B2 phases using lab-scale XRD. Therefore, further TEM characterizations are needed to determine the order/disorder information of a specific phase, to be discussed later.

Further SEM characterization in Figure 2a reveals that constituent phases in the as-cast $Ni_{49}Fe_{28}Al_{17}V_6$ EHEA are primarily manifest as nanolamellar structures. No preferred orientation or crystallographic texture was observed in these lamellar eutectic colonies, as revealed by the EBSD inverse pole figure (IPF) map in Figure 2b. We also observed trace non-lamellar eutectic colonies in the inter-dendritic regions, which is likely due to the

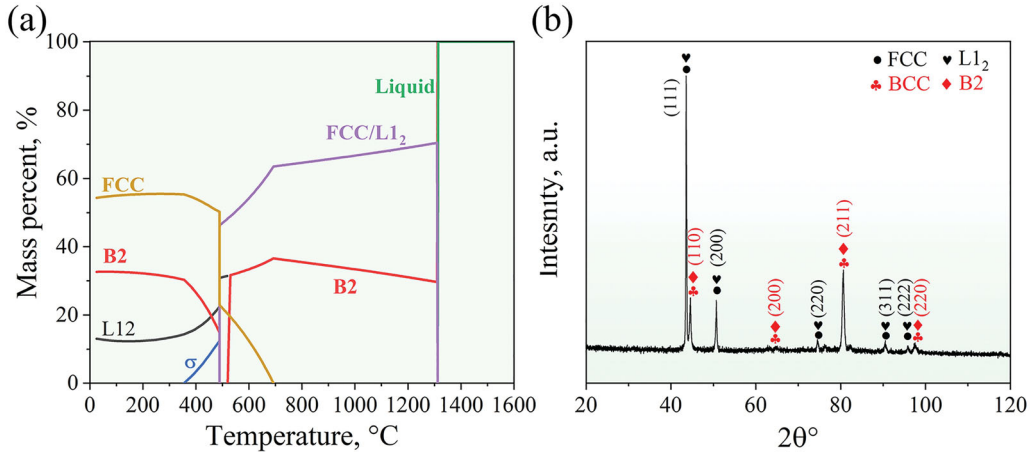

Figure 1. (a) Phase equilibria diagram showing phase constitute of $Ni_{49}Fe_{28}Al_{17}V_6$ as a function of temperature. (b) XRD pattern of the as-cast $Ni_{49}Fe_{28}Al_{17}V_6$ EHEA.

solidification instabilities induced by local compositional fluctuations or different growth rates of the dual phases [18,19]. The respective area fractions of FCC/$L1_2$ and BCC/B2 phases are approximately 72.5% and 27.5%, as revealed by the EBSD phase map (Figure 2c), which agrees well with our CALPHAD prediction (Figure 1a). Note that EBSD characterization cannot identify order/disorder information of a specific phase, and therefore here we resort to TEM characterization. A typical lamellar eutectic morphology is revealed by high-angle annular dark-field scanning transmission electron microscopy (HAADF-STEM), as shown in Figure 2d. The FCC and B2 nanolamellae have an average width of $\sim 550 \pm 80$ and 330 ± 45 nm, respectively. The selected area electron diffraction (SAED) patterns in Figure 2e and f indicate that both nanolamellae have ordering features, as shown by the superlattice spots. Figure 2g is a high-resolution TEM (HRTEM) image of the coarser nanolamellae (in yellow circle), with the inset of a corresponding fast Fourier transform (FFT) pattern showing superlattice reflections. The inverse fast Fourier transform (IFFT) image in Figure 2 h was obtained using the $1\bar{1}0$ and $00\bar{1}$ superlattice reflections, which clearly confirms the presence of ordered $L1_2$ domains (bright contrast) of 1–4 nm in diameters uniformly distributed in the FCC matrix. The formation of the $L1_2$ domains possibly originates from spinodal decomposition of FCC phase [20–22]. The HRTEM image of the finer nanolamellae (in blue circle in Figure 2d) in Figure 2i shows the atomic structure of the ordered B2 phase. The corresponding FFT diffraction pattern indicates the strong B2 reflection and provides chemical ordering information. No precipitates were observed in the B2 nanolamellae. Figure 2k displays that the $(1\bar{1}1)$ spot of the FCC phase coincides with the $(10\bar{1})$ spot of the B2 phase, which was collected from both FCC and B2 phases (Figure 2j). Thus, a classical Kurdjumov-Sachs (K-S) orientation relationship is established between FCC and B2 phases, namely, $(1\bar{1}1)_{FCC}//(10\bar{1})_{B2}$ and $[110]_{FCC}//[111]_{B2}$. As shown in Figure 2 l, a rough interface of the FCC and B2 phases was revealed via a HRTEM image at the atomic scale, which is a typical feature of non-faceted eutectic growth [23]. Figure 2m shows an IFFT image of the semi-coherent phase interface that is accompanied by lattice misfit dislocations. In addition, the FCC nanolamellae are rich in Fe and V elements, while the B2 nanolamellae are enriched by Al and Ni elements, as revealed by STEM energy-dispersive spectroscopy (EDS) mapping (Figure 2n). The specific chemical compositions of the FCC, $L1_2$, and B2 phases are listed in Table 1.

Table 1. Chemical compositions (at.%) of as-cast $Ni_{49}Fe_{28}Al_{17}V_6$ EHEA based on STEM-EDS analysis.

	Compositions (at.%)			
Phases	Ni	Fe	Al	V
FCC	50.65 ± 0.26	32.42 ± 0.23	8.90 ± 0.11	8.03 ± 0.09
$L1_2$	61.18 ± 0.29	22.57 ± 0.22	12.39 ± 0.13	3.84 ± 0.06
B2	53.45 ± 0.36	20.79 ± 0.21	21.83 ± 0.14	3.93 ± 0.08

Figure 3a shows the tensile engineering stress–strain curve of the as-cast $Ni_{49}Fe_{28}Al_{17}V_6$ EHEA, which exhibits a tensile yield strength ($\sigma_{0.2}$) of 760 ± 11 MPa and an ultimate tensile strength (σ_u) of 1290 ± 23 MPa. We also observed remarkable strain hardening rates in the plastic regime (Figure 3a inset), giving rise to a large uniform elongation ($_u$) of $\sim$ 26%. Figure 3b shows a direct comparison of our as-cast $Ni_{49}Fe_{28}Al_{17}V_6$ EHEA with other state-of-the-art cast EHEAs [8,24–33]. The tensile properties of our as-cast $Ni_{49}Fe_{28}Al_{17}V_6$ EHEA

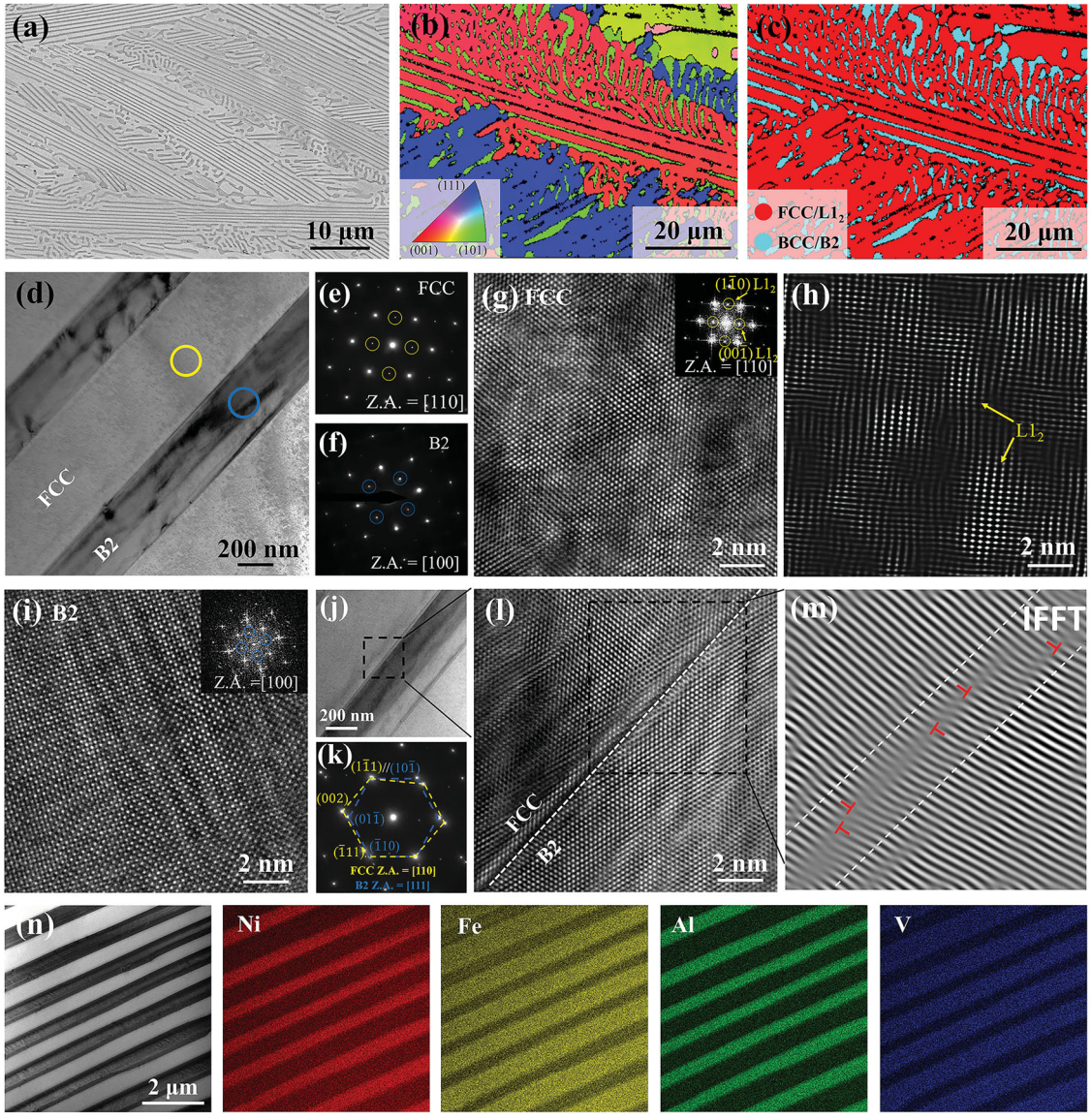

Figure 2. Microstructure of the as-cast $Ni_{49}Fe_{28}Al_{17}V_6$ EHEA. (a) SEM image. (b) EBSD IPF map. (c) EBSD phase map. (d, e, f) HAADF-STEM image, and corresponding SAED patterns with superlattice diffraction spots marked by circles. (g) HRTEM image along [110] zone axis of the FCC matrix phase, with the inset of an FFT image. (h) IFFT image derived from (g) using 001 and $\bar{1}10$ superlattice reflections of $L1_2$ domains. (i) HRTEM image of B2 nanolamellae with the inset of an FFT pattern. (j, k) Enlarged HAADF-STEM image of FCC and B2 nanolamellae and the corresponding SAED pattern, showing a semi-coherent interface with $(1\bar{1}1)_{FCC}//(10\bar{1})_{B2}$. (l) HRTEM image of a typical lamellar interface at the atomic scale. The phase interface is marked by a white dotted line. (m) IFFT image of the marked region in (l). ⊥, misfit dislocation. (n) HAADF-STEM image and corresponding EDS elemental maps of Ni, Fe, Al, and V.

surpass those of existing as-cast EHEAs. Notably, the as-cast $Ni_{49}Fe_{28}Al_{17}V_6$ EHEA has a high specific tensile strength of $\sim$ 186MPa·cm^3 g^{-1}, which is also substantially higher than those of other high-performing as-cast EHEAs (Figure 3c). Moreover, we constructed the map of the product of σ_u and fracture elongation ($_f$) ($\sigma_u \times {}_f$) vs. $\sigma_{0.2}$ as a measure of energy absorption capacity in Figure 3d, which demonstrates that the as-cast $Ni_{49}Fe_{28}Al_{17}V_6$ EHEA in our study has a high value of $\sigma_u \times {}_f$ (34.19 GPa·%), far outperforming other as-cast EHEAs [8,24–33]. In order to understand the fracture mechanism of the as-cast $Ni_{49}Fe_{28}Al_{17}V_6$ EHEA, the tensile fracture morphology was carefully characterized. The slip/shear bands, abundant dimple patterns, and secondary cracks, etc. were observed, which are typical characteristics of ductile fracture (see Supplementary material and Figure S2 for more details on fracture mechanisms).

To decipher the origin of the robust work hardening capability and the superior strength-ductility synergy of our $Ni_{49}Fe_{28}Al_{17}V_6$ EHEA, we carefully examined the deformation substructures of the fractured sample after

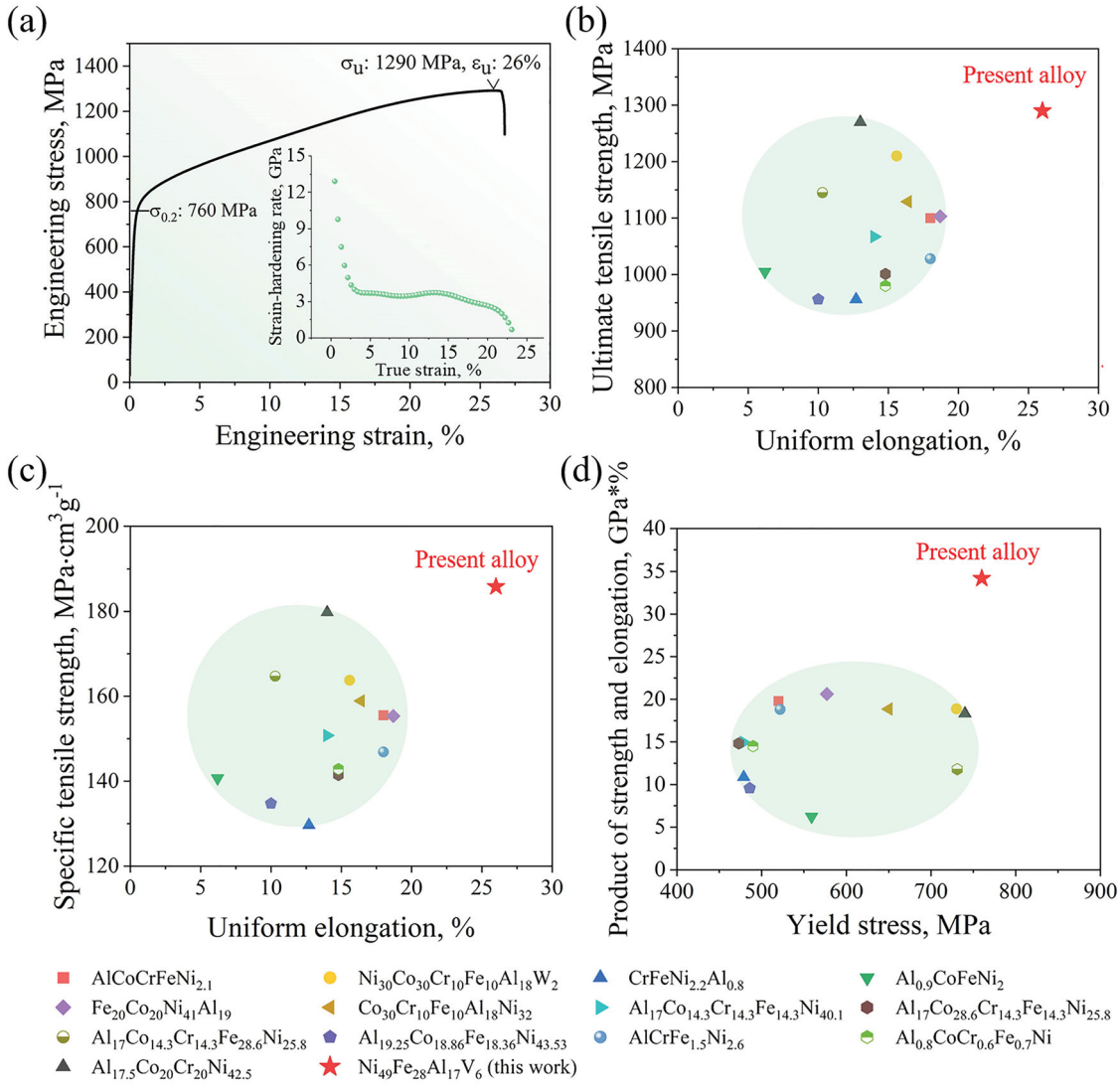

Figure 3. (a) Tensile stress-strain curve of the as-cast $Ni_{49}Fe_{28}Al_{17}V_6$ EHEA at ambient temperature. The inset shows the corresponding strain hardening rate versus true strain curve. Comparison of the mechanical properties of our as-cast $Ni_{49}Fe_{28}Al_{17}V_6$ EHEA with those of other high-performing EHEAs [8,24–33]: (b) Ultimate tensile strength versus uniform elongation. (c) Specific strength versus uniform elongation. (d) Yield strength versus the product of strength and ductility. The tensile properties of the previously reported EHEAs are summarized in Supplementary Table S1.

tension. The dual-phase eutectic structure of alternating soft FCC and hard B2 nanolamellae was maintained during tensile straining, with both nanolamellae being filled by a high density of dislocations (Figure 4a). The EBSD characterization on the fracture region also confirmed the high-density dislocations in both FCC and B2 lamellae (Supplementary Figure S3). Significantly, the FCC phase shows a higher dislocation density than the B2 phase, as shown in the KAM map and KAM distribution plots (Supplementary Figure S3c and e). Such findings are similar to the dislocation distribution between FCC and B2 BCC in as-cast $AlCoCrFeNi_{2.1}$ EHEA observed by high-energy synchrotron X-ray diffraction [34]. An ultrahigh density of dislocations is piled up at the lamellar interfaces, as indicated by the white arrows in Figure 4b. In general, for such dual-phase lamellar-structured EHEAs, the soft lamellae deform plastically first during deformation, leading to a significant dislocation multiplication [35–37]. Nevertheless, the plastic deformation of these soft lamellae can be impeded by hard lamellae, triggering a significant dislocation pile-up at the phase interfaces [26,35,37–40]. In the present $Ni_{49}Fe_{28}Al_{17}V_6$ EHEA, the semi-coherent phase interfaces are strong enough to pin massive dislocations, resulting in accumulation of an ultra-high density of dislocations at the phase interfaces [23,41]. These interfacial dislocations are known as geometrically necessary dislocations (GNDs), which not only generate back-stress hardening but also help activate plastic deformation of the hard B2 lamellae [37,38,42–46]. Moreover, the K-S type orientation

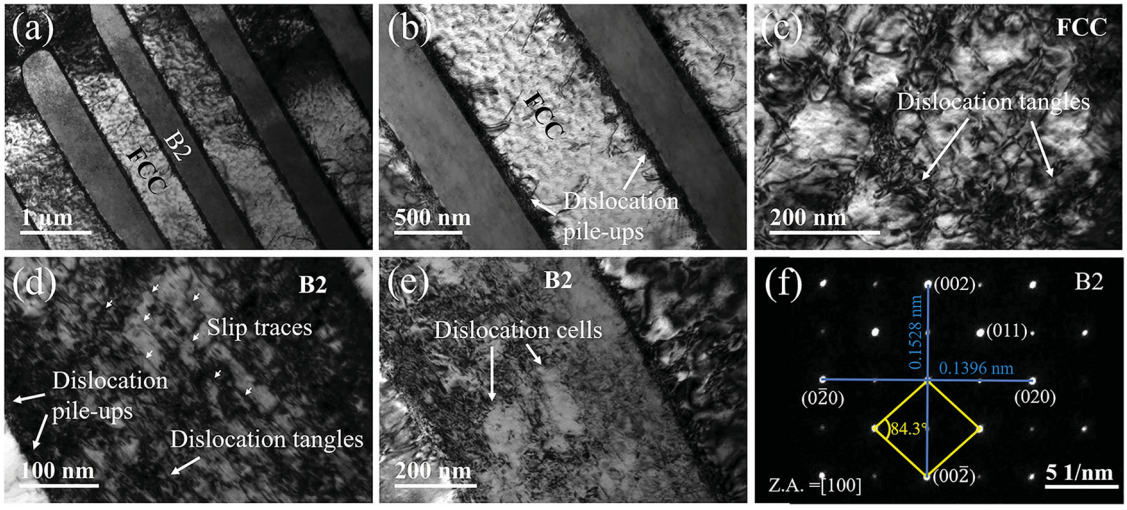

Figure 4. TEM images of the deformation microstructures after tensile fracture of the $Ni_{49}Fe_{28}Al_{17}V_6$ EHEA. (a) Low-magnification TEM image of the fractured nanolamellar structure. (b) Magnified TEM image showing the dislocation pile-ups at the nanolamellar interface. (c) Dislocation tangles in FCC phase. (d) Dislocation pile-ups, dislocation tangles, and slip traces in B2 phase. (e) Dislocation cells in B2 phase. (f) SAED pattern of the original B2 phase in the fractured sample taken from the zone axis of [100], manifesting the BCT crystal structure after deformation.

relationship can facilitate the slip transfer from the FCC nanolamellae to the B2 nanolamellae, which facilitates plastic co-deformation of the two constituent phases and thus contributes to the excellent strain-hardening capability [23]. Furthermore, we observed profuse dislocation tangles in the FCC nanolamellae (Figure 4c), possibly stemming from the strong interactions between dislocations in the FCC matrix and the $L1_2$ domains [47]. In addition, abundant straight (110) slip traces through B2 nanolamellae were also observed (Figure 4d), featuring a planar slip manner. The appearance of dislocation tangles in the B2 phase (Figure 4d) is presumably formed by the activation of massive cross slips [48]. A recent work by Chen et al. [35] also reported that the activation of the cross slips in the B2 phase of $AlCoCrFeNi_{2.1}$ EHEA mitigates local stress concentrations during the early stage of plastic deformation and promotes work hardening. Inspection of Figure 4e shows that the B2 phase in the $Ni_{49}Fe_{28}Al_{17}V_6$ EHEA after tensile fracture has elongated dislocation cell structures and dislocation tangles within the cell structures. The formation of the elongated dislocation cells may arise from dislocation overlap and crisscross interactions during straining [49,50]. The tangling of high-density dislocations can generate a considerable strain hardening effect to postpone necking instability. Consequently, these observations support steady strain hardening rates, as shown earlier in Figure 3. Of particular interest, we observed that the B2 phase underwent a phase transition into a body-centered tetragonal (BCT) structure (a distorted BCC lattice with a slight change of the *a*/*c* ratio) after tension. As shown in Figure 4f, the SAED pattern taken from B2 nanolamellae transfers from square-arranged spots before deformation to parallelogram-arranged spots after deformation. It is generally considered that such deformation-induced martensitic transformation (B2→BCT) could be attributed to the nucleation and propagation of 110 twinning plane [51,52]. In the present alloy, we observed abundant dislocation activities in the fractured sample, but we did not detect any feature of deformation twins. Thus, it is possible that the deformation-induced twining has already transformed into martensite (BCT) in the fractured sample at such a high strain. The B2 → BCT phase transformation not only helps release local stress concentrations and promote sustained plastic deformation, but also interrupts dislocation motion, thus offering additional strain hardening capability of the transformed B2 phase [53]. In contrast, the SAED pattern taken from the FCC phase demonstrated that the phase structure was maintained after fracture, as shown in Supplementary Figure S4. Overall, the phase transformation in the present $Ni_{49}Fe_{28}Al_{17}V_6$ EHEA enhances the deformability of the B2 phase and promotes the cooperative deformation between the soft and the hard nanolamellae.

4. Conclusions

In summary, we developed a lightweight $Ni_{49}Fe_{28}Al_{17}V_6$ EHEA that is free of Co and refractory elements. The as-cast $Ni_{49}Fe_{28}Al_{17}V_6$ EHEA comprises of a dual-phase eutectic structure of alternating soft FCC and hard B2 nanolamellae and exhibits an enhanced strength-ductility synergy that far exceeds that of previously

reported as-cast EHEAs. The exceptional strength-ductility synergy stems from the extensive dislocation activities in both FCC and B2 nanolamellae as well as the martensitic transformation induced plasticity in the B2 nanolamellae. The developed lightweight and low-cost $Ni_{49}Fe_{28}Al_{17}V_6$ EHEA by direct casting provides significant potential for a myriad of structural applications.

Acknowledgements

Siyuan Peng acknowledges the finanical support from the Natural Science Foundation of Xiamen, China, (No. 3502Z202371022). Shuai Feng acknowledges the financial support from the China Scholarship Council (CSC NO. 201906840076).

Disclosure statement

No potential conflict of interest was reported by the author(s).

Data availability

Data will be made available on request.

References

[1] George EP, Raabe D, Ritchie RO. High-entropy alloys. Nat Rev Mater. 2019;4:515–534. doi:10.1038/s41578-019-0121-4

[2] Li W, Xie D, Li D, et al. Mechanical behavior of high-entropy alloys. Prog Mater Sci. 2021;118:100777, doi:10.1016/j.pmatsci.2021.100777

[3] Mooraj S, Chen W. A review on high-throughput development of high-entropy alloys by combinatorial methods. J Mater Inf. 2023;3:4, doi:10.20517/jmi.2022.41

[4] Yao K, Liu L, Ren J, et al. High-entropy intermetallic compound with ultra-high strength and thermal stability. Scr Mater. 2021;194:113674, doi:10.1016/j.scriptamat.2020.113674

[5] Lu Y, Dong Y, Jiang H, et al. Promising properties and future trend of eutectic high entropy alloys. Scr Mater. 2020;187:202–209. doi:10.1016/j.scriptamat.2020.06.022

[6] Baker I, Wu M, Wang Z. Eutectic/eutectoid multi-principle component alloys: a review. Mater Charact. 2019;147:545–557. doi:10.1016/j.matchar.2018.07.030

[7] Lu Y, Dong Y, Guo S, et al. A promising New class of high-temperature alloys: eutectic high-entropy alloys. Sci Rep. 2014;4:6200, doi:10.1038/srep06200

[8] Gao X, Lu Y, Zhang B, et al. Microstructural origins of high strength and high ductility in an $AlCoCrFeNi_{2.1}$ eutectic high-entropy alloy. Acta Mater. 2017;141:59–66. doi:10.1016/j.actamat.2017.07.041

[9] Jiang H, Han K, Gao X, et al. A new strategy to design eutectic high-entropy alloys using simple mixture method. Mater Des. 2018;142:101–105. doi:10.1016/j.matdes.2018.01.025

[10] Chung D, Ding Z, Yang Y. Hierarchical eutectic structure enabling superior fracture toughness and superb strength in $CoCrFeNiNb_{0.5}$ eutectic high entropy alloy at room temperature. Adv Eng Mater. 2019;21:1801060, doi:10.1002/adem.201801060

[11] He F, Wang Z, Cheng P, et al. Designing eutectic high entropy alloys of CoCrFeNiNbx. J Alloy Compd. 2016;656:284–289. doi:10.1016/j.jallcom.2015.09.153

[12] Rogal Ł, Morgiel J, Świątek Z, et al. Microstructure and mechanical properties of the new $Nb_{25}Sc_{25}Ti_{25}Zr_{25}$ eutectic high entropy alloy. Mater Sci Eng A. 2016;651:590–597. doi:10.1016/j.msea.2015.10.071

[13] Ai C, He F, Guo M, et al. Alloy design, micromechanical and macromechanical properties of $CoCrFeNiTa_x$ eutectic high entropy alloys. J Alloy Compd. 2018;735:2653–2662. doi:10.1016/j.jallcom.2017.12.015

[14] Mukarram M, Mujahid M, Yaqoob K. Design and development of CoCrFeNiTa eutectic high entropy alloys. J Mater Res Technol. 2021;10:1243–1249. doi:10.1016/j.jmrt.2020.12.042

[15] Ding ZY, He QF, Wang Q, et al. Superb strength and high plasticity in laves phase rich eutectic medium-entropy-alloy nanocomposites. Int J Plast. 2018;106:57–72. doi:10.1016/j.ijplas.2018.03.001

[16] Shafiei A. Design of eutectic high entropy alloys in Al–Co–Cr–Fe–Ni system. Met Mater Int. 2021;27:127–138. doi:10.1007/s12540-020-00655-3

[17] Yin B, Maresca F, Curtin WA. Vanadium is an optimal element for strengthening in both fcc and bcc high-entropy alloys. Acta Mater. 2020;188:486–491. doi:10.1016/j.actamat.2020.01.062

[18] Lozinko A, Mishin OV, Yu T, et al. Quantification of microstructure in a eutectic high entropy alloy $AlCoCrFeNi_{2.1}$. IOP Conf Ser. 2019;580:012039, doi:10.1088/1757-899X/580/1/012039

[19] Lozinko A, Zhang Y, Mishin OV, et al. Microstructural characterization of eutectic and near-eutectic AlCoCrFeNi high-entropy alloys. J Alloy Compd. 2020;822:153558, doi:10.1016/j.jallcom.2019.153558

[20] Viswanathan GB, Banerjee R, Singh A, et al. Precipitation of ordered phases in metallic solid solutions: a synergistic clustering and ordering process. Scr Mater. 2011;65:485–488. doi:10.1016/j.scriptamat.2011.06.002

[21] Miao J, Slone C, Dasari S, et al. Ordering effects on deformation substructures and strain hardening behavior of a CrCoNi based medium entropy alloy. Acta Mater. 2021;210:116829, doi:10.1016/j.actamat.2021.116829

[22] Rojhirunsakool T, Singh ARP, Nag S, et al. Temporal evolution of non-equilibrium γ' precipitates in a rapidly quenched nickel base superalloy. Intermetallics. 2014;54:218–224. doi:10.1016/j.intermet.2014.06.011

[23] Xiong T, Yang W, Zheng S, et al. Faceted Kurdjumov-Sachs interface-induced slip continuity in the eutectic high-entropy alloy, $AlCoCrFeNi_{2.1}$. J Mater Sci Technol. 2021;65:216–227. doi:10.1016/j.jmst.2020.04.073

[24] Wu Q, He F, Li J, et al. Phase-selective recrystallization makes eutectic high-entropy alloys ultra-ductile. Nat Commun. 2022;13:4697, doi:10.1038/s41467-022-32444-4

[25] Jin X, Bi J, Zhang L, et al. A new $CrFeNi_2Al$ eutectic high entropy alloy system with excellent mechanical properties. J Alloy Compd. 2019;770:655–661. doi:10.1016/j.jallcom.2018.08.176

[26] Jiang H, Qiao D, Jiao W, et al. Tensile deformation behavior and mechanical properties of a bulk cast

$Al_{0.9}CoFeN_{i2}$ eutectic high-entropy alloy. J Mater Sci Technol. 2021;61:119–124. doi:10.1016/j.jmst.2020.05.053

[27] Jin X, Zhou Y, Zhang L, et al. A novel $Fe_{20}Co_{20}Ni_{41}Al_{19}$ eutectic high entropy alloy with excellent tensile properties. Mater Lett. 2018;216:144–146. doi:10.1016/j.matlet.2018.01.017

[28] Yang Z, Wang Z, Wu Q, et al. Enhancing the mechanical properties of casting eutectic high entropy alloys with Mo addition. Appl Phys A. 2019;125:208, doi:10.1007/s00339-019-2506-z

[29] Jin X, Zhou Y, Zhang L, et al. A new pseudo binary strategy to design eutectic high entropy alloys using mixing enthalpy and valence electron concentration. Mater Des. 2018;143:49–55. doi:10.1016/j.matdes.2018.01.057

[30] Shi P, Li Y, Wen Y, et al. A precipitate-free AlCoFeNi eutectic high-entropy alloy with strong strain hardening. J Mater Sci Technol. 2021;89:88–96. doi:10.1016/j.jmst.2021.03.005

[31] Wu H, Xie J, Yang H, et al. A cost-effective eutectic high entropy alloy with an excellent strength–ductility combination designed by VEC criterion. J Mater Res Technol. 2022;19:1759–1765. doi:10.1016/j.jmrt.2022.05.165

[32] Ma L, Wang J, Jin P. Microstructure and mechanical properties variation with Ni content in $Al_{0.8}CoCr_{0.6}Fe_{0.7}Ni_x$ ($x = 1.1, 1.5, 1.8, 2.0$) eutectic high-entropy alloy system. Mater Res Express. 2020;7:016566. doi:10.1088/2053-1591/ab6580

[33] Liu Q, Liu X, Fan X, et al. Designing novel AlCoCrNi eutectic high entropy alloys. J Alloy Compd. 2022;904:163775, doi:10.1016/j.jallcom.2022.163775

[34] Shen J, Lopes JG, Zeng Z, et al. Deformation behavior and strengthening effects of an eutectic $AlCoCrFeNi_{2.1}$ high entropy alloy probed by in-situ synchrotron X-ray diffraction and post-mortem EBSD. Mater Sci Eng A. 2023;872:144946, doi:10.1016/j.msea.2023.144946

[35] Chen J-X, Li T, Chen Y, et al. Ultra-strong heavy-drawn eutectic high entropy alloy wire. Acta Mater. 2023;243:118515, doi:10.1016/j.actamat.2022.118515

[36] Bhattacharjee T, Wani IS, Sheikh S, et al. Simultaneous strength-ductility enhancement of a nano-lamellar $AlCoCrFeNi_{2.1}$ eutectic high entropy alloy by cryo-rolling and annealing. Sci Rep. 2018;8:3276, doi:10.1038/s41598-018-21385-y

[37] Shi P, Zhong Y, Li Y, et al. Multistage work hardening assisted by multi-type twinning in ultrafine-grained heterostructural eutectic high-entropy alloys. Mater Today. 2020;41:62–71. doi:10.1016/j.mattod.2020.09.029

[38] Shi P, Li R, Li Y, et al. Hierarchical crack buffering triples ductility in eutectic herringbone high-entropy alloys. Science. 2021;373:912–918. doi:10.1126/science.abf6986

[39] Wang J, Misra A. Plastic homogeneity in nanoscale heterostructured binary and multicomponent metallic eutectics: an overview. Curr Opin Solid State Mater Sci. 2023;27:101055, doi:10.1016/j.cossms.2022.101055

[40] Gao YF, Zhang W, Shi PJ, et al. A mechanistic interpretation of the strength-ductility trade-off and synergy in lamellar microstructures. Mater Today Adv. 2020;8:100103, doi:10.1016/j.mtadv.2020.100103

[41] Xu N, Yang Z, Mu X, et al. Effect of Al addition on the microstructures and deformation behaviors of non-equiatomic FeMnCoCr metastable high entropy alloys. Appl Phys Lett. 2021;119:261902, doi:10.1063/5.0069518

[42] Shi P, Ren W, Zheng T, et al. Enhanced strength–ductility synergy in ultrafine-grained eutectic high-entropy alloys by inheriting microstructural lamellae. Nat Commun. 2019;10:489, doi:10.1038/s41467-019-08460-2

[43] Jiang Z, Chen W, Chu C, et al. Directly cast fibrous heterostructured $FeNi_{0.9}Cr_{0.5}Al_{0.4}$ high entropy alloy with low-cost and remarkable tensile properties. Scr Mater. 2023;230:115421. doi:10.1016/j.scriptamat.2023.115421

[44] Wu X, Zhu Y. Heterogeneous materials: a new class of materials with unprecedented mechanical properties. Mater Res Lett. 2017;5:527–532. doi:10.1080/21663831.2017.1343208

[45] Wu X, Yang M, Yuan F, et al. Heterogeneous lamella structure unites ultrafine-grain strength with coarse-grain ductility. Proc Natl Acad Sci USA. 2015;112:14501–14505. doi:10.1073/pnas.1517193112

[46] Zhu Y, Ameyama K, Anderson PM, et al. Heterostructured materials: superior properties from hetero-zone interaction. Mater Res Lett. 2021;9:1–31. doi:10.1080/21663831.2020.1796836

[47] Ovri H, Lilleodden ET. New insights into plastic instability in precipitation strengthened Al–Li alloys. Acta Mater. 2015;89:88–97. doi:10.1016/j.actamat.2015.01.065

[48] Picak S, Yilmaz HC, Karaman I. Simultaneous deformation twinning and martensitic transformation in CoCrFeMnNi high entropy alloy at high temperatures. Scr Mater. 2021;202:113995, doi:10.1016/j.scriptamat.2021.113995

[49] Guo W, Su J, Lu W, et al. Dislocation-induced breakthrough of strength and ductility trade-off in a non-equiatomic high-entropy alloy. Acta Mater. 2020;185:45–54. doi:10.1016/j.actamat.2019.11.055

[50] Yan X, Liaw PK, Zhang Y. Ultrastrong and ductile BCC high-entropy alloys with low-density via dislocation regulation and nanoprecipitates. J Mater Sci Technol. 2022;110:109–116. doi:10.1016/j.jmst.2021.08.034

[51] Park HS. Stress-Induced martensitic phase transformation in intermetallic nickel aluminum nanowires. Nano Lett. 2006;6:958–962. doi:10.1021/nl060024p

[52] Sutrakar VK, Mahapatra DR. Single and multi-step phase transformation in CuZr nanowire under compressive/tensile loading. Intermetallics. 2010;18:679–687. doi:10.1016/j.intermet.2009.11.006

[53] Wen X, Zhu L, Naeem M, et al. Strong work-hardenable body-centered-cubic high-entropy alloys at cryogenic temperature. Scr Mater. 2023;231:115434, doi:10.1016/j.scriptamat.2023.115434